

Enhanced EUV Mask Imaging Using Fourier Ptychographic Microscopy

Chaoying Gu^a, Antoine Islegen-Wojdyla^b, Markus Benk^b, Kenneth A. Goldberg^b, and Laura Waller^a

^aDepartment of Electrical Engineering and Computer Sciences, University of California, Berkeley; Berkeley, CA, 94704, USA

^bLawrence Berkeley National Laboratory, Berkeley, CA, 94720, USA

ABSTRACT

Extreme Ultraviolet (EUV) mask imaging requires higher resolution and phase sensitivity for next-generation lithography. This work explores Fourier Ptychographic Microscopy (FPM) as a solution, addressing challenges such as field-dependent aberrations outside of the microscope's designed field-of-view (FOV) for 1D and 2D patterns. Using binary pseudo-random mask patterns (BPRP) and various reconstruction algorithms, we achieve a 1.8× enhancement beyond the $0.5\lambda/\text{NA}$ resolution limit, improving the resolved feature size from 82 nm to 46 nm across a $30\ \mu\text{m} \times 30\ \mu\text{m}$ FOV. FPM's phase reconstruction also enables arbitrary illumination synthesis, allowing for the computational emulation of diverse illumination patterns from a single FPM dataset. These results demonstrate FPM's potential as a powerful computational imaging tool for high-NA EUV mask imaging and metrology.

Keywords: Fourier Ptychography, Extreme ultraviolet lithography, Aperture synthesis, Full-field imaging, Aberration reconstruction, Fresnel zoneplates, photomasks, Computational imaging

1. INTRODUCTION

The performance of an imaging system is fundamentally governed by its optical components, particularly the lenses, which determine key attributes such as light efficiency, resolution, and aberrations. Phase retrieval and aperture synthesis mitigate these limitations by computationally combining multiple images captured under different illumination conditions, effectively extending the numerical aperture and enabling computational aberration correction. This technique, widely employed in fields like radar and astronomy, has also been adapted to microscopy.

Fourier Ptychographic Microscopy (FPM)¹ is a computational imaging method that reconstructs a high-resolution complex-valued image by computationally stitching multiple shifted apertures in the Fourier domain. By acquiring multiple intensity images under varying illumination angles, the complex-field image and pupil are computationally reconstructed. Leveraging redundant spatial frequency information in overlapping regions, FPM enables high-resolution reconstruction beyond the $0.5\lambda/\text{NA}$ resolution limit of the objective lens and quantitative phase imaging, making it a powerful tool for high-resolution, phase-sensitive applications. FPM has gained significant traction in optics, enabling quantitative phase imaging for both 2D microscopy² and 3D diffraction tomography.³ Beyond visible-light applications, FPM has also been extended to X-ray microscopy, where it has demonstrated unexpected dose efficiency.⁴

This work extends the application of FPM to the extreme ultraviolet (EUV) spectrum, with a focus on enhancing the capabilities of the SHARP High-NA Actinic Reticle Review Project (SHARP) EUV microscope. SHARP is a synchrotron-based EUV microscope operating at 13.5 nm at Lawrence Berkeley National Laboratory's Advanced Light Source. Fig. 1 shows the layout of the tool. It features highly tunable imaging capabilities, including user-selectable Fresnel zone plate objectives⁵ and a Fourier-synthesis illuminator.^{6,7} SHARP can emulate a variety of current and future lithography tool numerical apertures and illumination properties, making it an ideal platform for evaluating mask architectures and imaging performance in high-NA EUV lithography.⁸

Further author information:

Chaoying Gu: E-mail: chaoying_gu@berkeley.edu

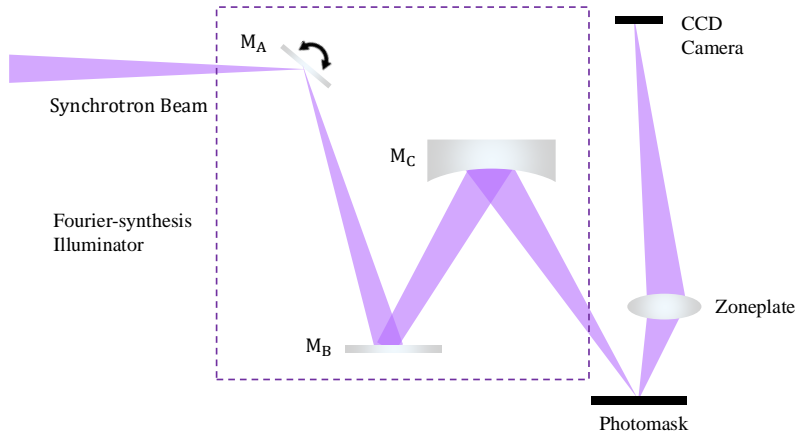


Figure 1. SAHRP layout. A low-divergence synchrotron beam is first directed onto a flat turning mirror M_A , which redirects it toward the illuminator. The illuminator then images the beamline focus onto the photomask, providing critical illumination. Finally, the reflective mask is imaged onto a CCD camera using an off-axis zone plate lens. The Fourier-synthesis illuminator consists of the turning mirror M_A , a flat mirror M_B and a condenser M_C . The beam on the turning mirror is optically conjugated with the focus on the photomask, allowing precise beam steering across the aperture during exposure.

The key component for FPM is the Fourier-synthesis illuminator, which provides flexible coherence control by scanning illumination angles through an optically conjugated condenser system.^{8,9} This allows for precise angular diversity in the illumination, making it well-suited for Fourier-domain aperture synthesis techniques like FPM.

Previous studies⁹ have demonstrated FPM for the diffraction-limited central imaging region in SHARP, but its applicability to the full field-of-view (FOV) and regions affected by field-dependent aberrations remained unexplored. In this work, we expand its scope by conducting a systematic aberration tolerance analysis, incorporating various measurement schemes and reconstruction algorithms to assess FPM's robustness under spatially-varying aberrations.

To improve the performance of FPM and expand the usable FOV, we explore different optimization methods, employing automatic differentiation and regularization techniques to enhance reconstruction quality beyond the central imaging region. Additionally, we demonstrate FPM reconstructions with high-NA zone plates and 2D patterns, showcasing its ability to recover complex spectral information. This capability enables arbitrary illumination synthesis and defocus behavior simulation, crucial for EUV mask imaging and metrology.

2. FORWARD MODEL

Under the thin-sample approximation, the intensity of the n -th measurement $I_n(x, y)$ in Fourier ptychography is modeled as follows. The object is represented by its complex-field transmission function $O(x, y)$, which has a corresponding Fourier spectrum $\hat{O}(k_x, k_y)$. In the n -th measurement, the sample is illuminated by a plane wave with wave-vector components (k_{xn}, k_{yn}) , shifting the object's spectrum accordingly. The pupil function $P(k_x, k_y)$ of the imaging system acts as a bandpass filter, selecting a finite region of the shifted spectrum for image formation.

Mathematically, the n -th FP measurement is given by:

$$I_n(x, y) = \left| \mathcal{F}^{-1} \left\{ P(k_x, k_y) \cdot \hat{O}(k_x - k_{xn}, k_y - k_{yn}) \right\} \right|^2 \quad (1)$$

where \mathcal{F}^{-1} denotes the inverse Fourier transform,

In Fourier ptychography, multiple measurements are acquired under varying illumination angles, which correspond to different spectrum shifts. By combining these measurements in an iterative phase retrieval process,

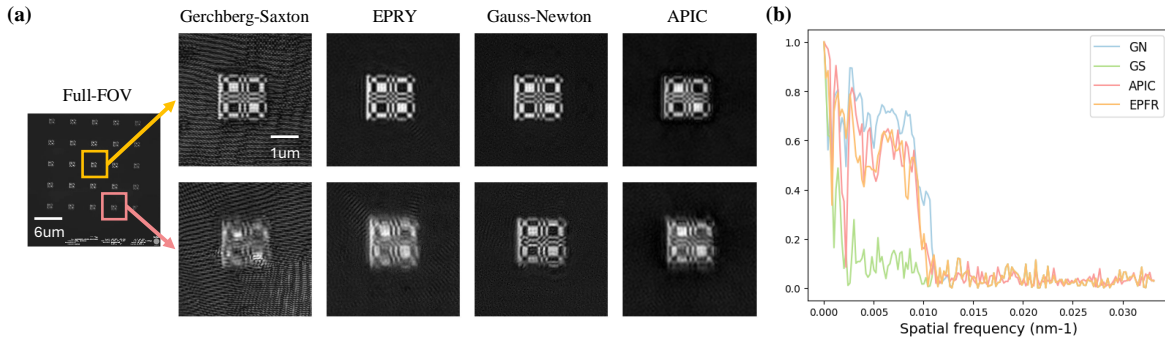


Figure 2. Comparison across different reconstruction algorithms. (a) Fourier Ptychography amplitude reconstructions of two sample regions (central region in orange and corner region in red) in the FoV, using using various algorithms: Gerchberg-Saxton (GS), Embedded Pupil Function Recovery (EPRY), Gauss-Newton (GN) and Angular ptychographic imaging with closed-form method (APIC). (b) The Fourier Ring Correlation curve between the reconstructions of the corner patch by different algorithms and the highest quality central patch reconstruction (specifically, the GN result in the top row of panel (a)).

one can computationally recover a high-resolution estimate of $\hat{O}(k_x, k_y)$ that extends beyond the passband of the pupil function, achieving resolution beyond the $0.5\lambda/\text{NA}$ limit of the objective lens.

3. METHODS

3.1 Reconstruction algorithms

We evaluate the performance of four distinct algorithms: the First-order Gerchberg-Saxton (GS),¹ Embedded Pupil Function Recovery (EPRY),¹⁰ Second-order Gauss-Newton (GN),¹¹ and Angular ptychographic imaging with closed-form method (APIC).¹² Fig. 2 shows the results.

The GS algorithm is applied to reconstruct images without aberration or when a ground truth aberration is provided, without solving for the aberration itself. Conversely, EPRY estimates both the object and the pupil function simultaneously; it exhibits slow convergence, yet faithfully reconstructs the aberrations. A survey study by Yeh, *et al.*¹³ concluded that the GN method, with its pupil estimation capability, typically offers superior results in the presence of aberrations. Notably, GN's main advantages are its robustness to systematic errors and rapid convergence.

APIC is a recently proposed method that aims to produce robust and fast FPM reconstructions analytically.¹² Nonetheless, it faces significant challenges in the EUV measurement context. First, APIC assumes absorptive objects with strong DC components, but EUV masks are reflective objects with a weaker DC component. Second, APIC demands precise NA-matching data that aligns closely with the transition between bright-field and dark-field imaging. Its performance declines when the tolerance is increased to accommodate the illumination pattern employed in the EUV microscope.

3.2 Differentiable optimization

To enhance reconstruction quality, we apply automatic differentiation (AD), a computational technique that enables efficient gradient-based optimization. Automatic differentiation automatically computes analytic derivatives with respect to model parameters by constructing a computational graph, eliminating the need for manual derivation of gradients. It has been applied to spatial-domain ptychography¹⁴ and also Fourier ptychography.¹⁵

We evaluate two optimization objectives in our framework. The first is the amplitude loss, originally suggested by Yeh *et al.*,¹³ which directly minimizes the discrepancy between the measured and reconstructed amplitudes:

$$\mathcal{L}_{oss_{amp}} = \sum_{n=1}^N \left| \sqrt{I_n} - \left| \mathcal{F}^{-1} \left\{ P(k_x, k_y) \cdot \hat{O}(k_x - k_{xn}, k_y - k_{yn}) \right\} \right| \right|. \quad (2)$$

The second objective is feature-domain loss, which minimizes the discrepancy in the first-order gradient of the images:

$$\mathcal{L}_{oss_{feature}} = \sum_{n=1}^N \left| \nabla \sqrt{I_n} - \nabla \left| \mathcal{F}^{-1} \left\{ P(k_x, k_y) \cdot \hat{O}(k_x - k_{xn}, k_y - k_{yn}) \right\} \right| \right|. \quad (3)$$

While feature-domain loss has been reported to enhance robustness against system errors such as vignetting, stray light artifacts, illumination intensity variations, and positional inaccuracies,¹⁶ we found that continued optimization with this objective can cause the amplitude loss to explode and thus distort the reconstruction. As a result, we did not use feature-domain loss in our final reconstruction.

In addition to automatic differentiation-based optimization, we incorporate total-variation (TV) regularization on the reconstructed pupil function¹⁷ as a separate enhancement technique. This regularization can improve reconstruction quality, particularly in regions affected by aberrations and vignetting. The results, shown in Fig. 4, demonstrate that automatic differentiation, combined with pupil regularization, significantly enhances contrast and reconstruction stability, particularly in highly-aberrated regions.

3.3 Fourier Ring Correlation evaluation

In visible-light applications, a higher-NA lens is often used to provide a reference for a ground truth comparison. In this work, since the object consists of a repetitive pattern array, we instead assess reconstruction quality by analyzing the correlation between the center and corner patches using Fourier ring correlation (FRC).¹⁸ This approach provides a quantitative measure of reconstruction performance in the absence of a higher-NA reference.

FRC is a quantitative measure of similarity between two images in the frequency domain, expressed as a function of spatial frequency. The FRC plots provide a detailed analysis of how different frequency components contribute to the overall image reconstruction quality. It is defined by the following equation:

$$\text{FRC}(R) = \frac{\tilde{I}_1(R) \cdot \tilde{I}_2(R)^*}{\sqrt{|\tilde{I}_1(R)|^2 \cdot |\tilde{I}_2(R)|^2}}, \quad (4)$$

where R represents a specific spatial frequency within radius R in the frequency domain, and $\tilde{I}_1(R)$ and $\tilde{I}_2(R)$ are the Fourier transforms of two images extracted at radius R and treated as a 1D vector, and $*$ denotes the complex conjugate.

Figure 2 (b) presents the FRC curves for the different reconstruction algorithms described in Sec. 3.1, comparing the corner patch reconstruction against the highest-quality central patch reconstruction. The results demonstrate that the Gauss-Newton algorithm outperforms the others in handling field-dependent aberrations in the peripheral regions, achieving better consistency and resolution across the full field of view.

4. EXPERIMENTS

4.1 Extended usable FOV

We use experimental data acquired on the SHARP EUV microscope. The object under investigation is a 5×5 array of binary pseudo-random patterns (BPRP). Each individual pattern in the array measures $1.14 \mu\text{m}$ per side with a line width of 60 nm .

BPRP samples are well-suited for validating full-FOV aberration characterization. They provide a broad spectral coverage that effectively probes the entire pupil, whereas traditional resolution test patterns, such as USAF targets, primarily probe specific spatial frequencies. However, they are also challenging to fabricate—features below 60 nm often suffer from pattern collapse. We use BPRP for our investigation in order to characterize the imaging system of the microscope and thus correct the aberration for other mask imaging tasks.

The zoneplate used in our experiments has a mask-side NA of 0.082 matching the 0.33 NA generation of EUV lithography. The corresponding $0.5\lambda/\text{NA}$ resolution limit is 82 nm . The smallest feature size of the BPRP is 60 nm , which is below the resolution limit and should not be resolved in an image using low-sigma illumination.

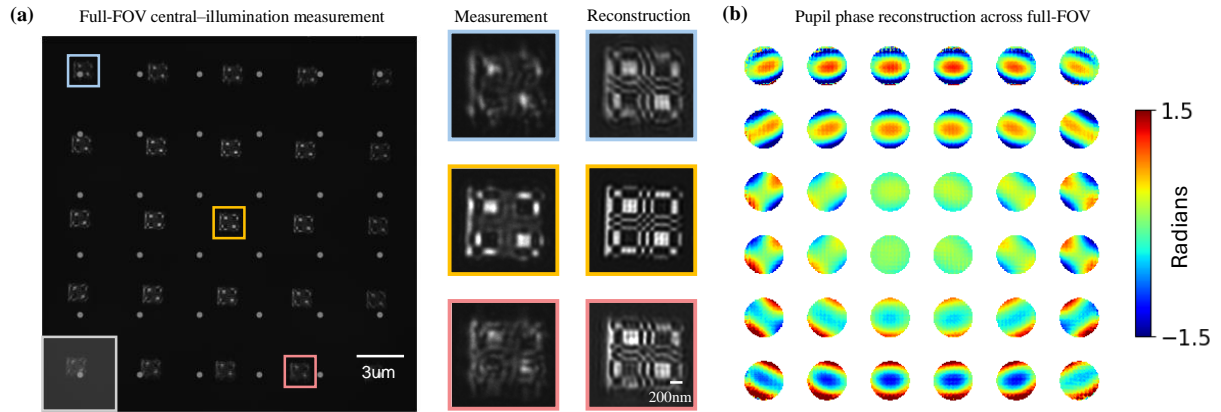


Figure 3. Full field-of-view Fourier Ptychography reconstruction of data collected at 13.5 nm wavelength. (a) Details of three sample regions in the full FOV, showing one raw captured image and the corresponding reconstruction for each. The gray box in the bottom left corner marks the patch used for field-dependent aberration analysis in panel (b). The gray dots indicate the centers of the segmented regions, with the full FOV divided into a 6×6 grid with 20% overlap. (b) Full-FOV aberration visualization, where the 6×6 grid layout presents the pupil wavefront reconstruction for each patch.

From the initial low-NA captures, depicted in the second column of Fig. 3 (a), it is evident that: 1. resolving the lines within the central 'sweet spot' region requires the use of off-axis illumination, or synthetic aperture techniques (enabled by FPM); 2. the corner regions of the FOV are degraded by field-dependent aberrations, requiring computational correction. After our implementation of full-FOV FPM reconstruction, both challenges are addressed as the last column of Fig. 3 (a) displays. Previously unresolved lines become clearly defined, and the local field-dependent aberrations are effectively deconvolved computationally.

In addition, we present the field-dependent pupil reconstruction in Fig. 3 (b). Previous studies have characterized the system's aberration using through-focus image stacks^{19,20} and speckle.²¹ Since different zoneplates and imaging settings were used in these studies, we did not perform a quantitative comparison of the reconstructed aberrations; however, the results qualitatively align.

We further demonstrate our approach using a large binary pseudo-random array (BPRA) sample made by HighRI Optics. The leftmost column of Fig. 4 presents the full-field FP reconstruction using the GN algorithm, which exhibits reduced illumination intensity outside the central imaging region and field-dependent aberrations inherited from the raw measurements.

To mitigate these issues, we apply automatic differentiation-based optimization, as described in Sec. 3.2. The right column of Fig. 4 compares the reconstructed object amplitude and pupil phase before and after AD optimization. A line section plot is included below to quantitatively illustrate the contrast enhancement achieved through optimization, demonstrating improved reconstruction quality in previously degraded regions.

4.2 System error correction

Co-optimizing the illumination vectors, as proposed by You et al.,¹⁵ is challenging due to the lack of well-parametrized constraints, making direct optimization difficult. Instead, we adopt a more systematic approach to model the illumination wavevector offsets that arise due to field-dependent systematic errors.

A well-known error in visible-light FPM is the misalignment of LED positions, which leads to variations in illumination angles. Unlike traditional LED-based systems, the SHARP EUV microscope employs an angle scanner and a condenser to generate tilted illumination. This design introduces additional sources of field-dependent illumination errors beyond simple angular misalignment. Prior studies on the SHARP system²¹ have reported that coherent illumination exhibits field-dependent angular variations due to a relative defocus between the illumination and object planes.

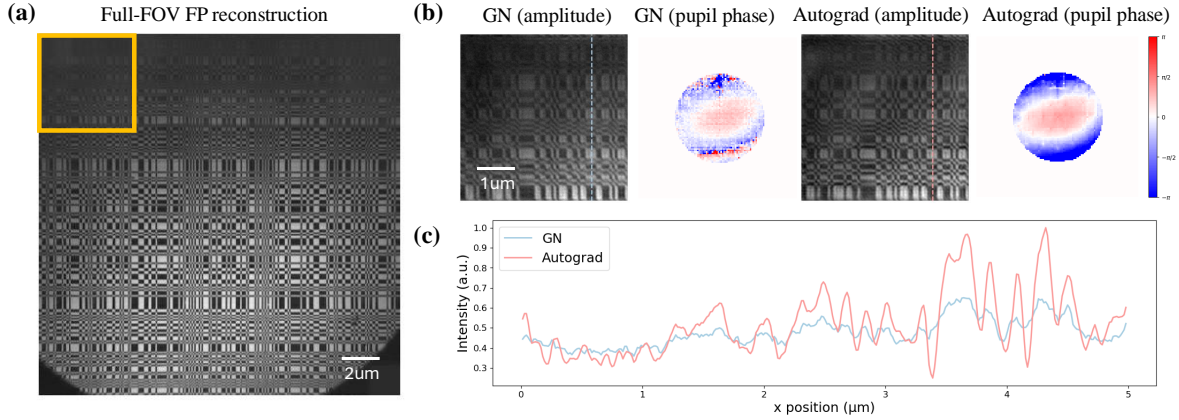


Figure 4. The automatic differentiation optimization for highly-aberrated region. (a) the full-field Fourier Ptychography reconstruction using the Gauss-Newton (GN) algorithm, where illumination roll-off and aberration effects remain strong. (b) The reconstructed object amplitude and pupil phase before (left) and after (right) automatic differentiation optimization. (c) A line section of the reconstructed amplitude, corresponding to the lines in panel (b) to visualize the contrast enhancement quantitatively.

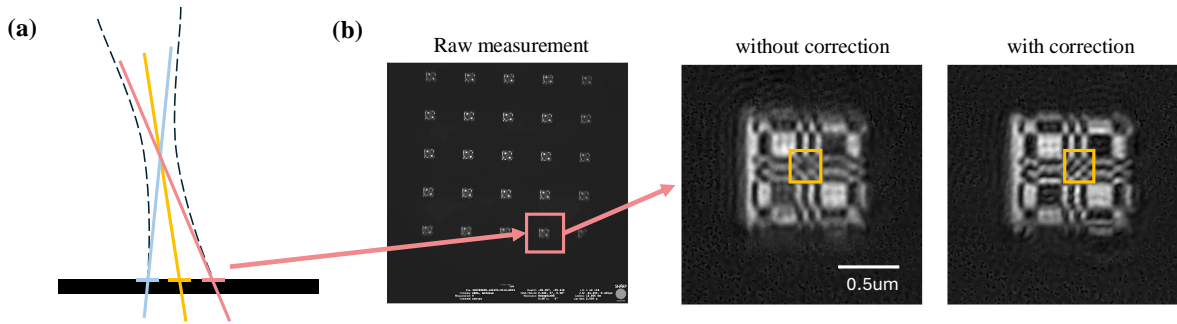


Figure 5. Systematic illumination error correction in the SHARP EUV system. (a) Front-view system diagram illustrating how an imperfect plane wave, modeled as a Gaussian beam, results in spatially varying illumination wave-vectors across the FOV. Different color-coded FOV regions correspond to distinct illumination wave-vectors, indicated by their respective colors. The black rectangle represents the sample plane. (b) Gauss-Newton reconstruction comparison, demonstrating improved resolution after correcting field-dependent illumination errors. The yellow square highlights dots that were unresolved before the correction but become more distinguishable afterward.

To account for these variations, we apply a first-order approximation and parameterize the field-dependent shift in the illumination wavevector as:

$$\vec{k}_t = \vec{k}_0 + \alpha \cdot \vec{x}_t, \quad (5)$$

where \vec{k}_t is the field dependent illumination vector at position \vec{x}_t , and \vec{k}_0 is the central illumination vector.

To determine the optimal correction, we use automatic differentiation to optimize α . Figure 5 illustrates the impact of this correction. The system diagram in Fig. 5(a) highlights how an imperfect planar wave (more accurately, a Gaussian beam) leads to varying illumination wavevectors across different regions of the FOV. The GN-based reconstruction comparison in Fig. 5(b) shows that after applying the correction, modulation is increased for the central features, indicating improved spatial coherence. Additionally, the FRC plot between the reconstruction and the central 'ground truth' shows an overall increase, confirming that the correction enhances reconstruction quality.

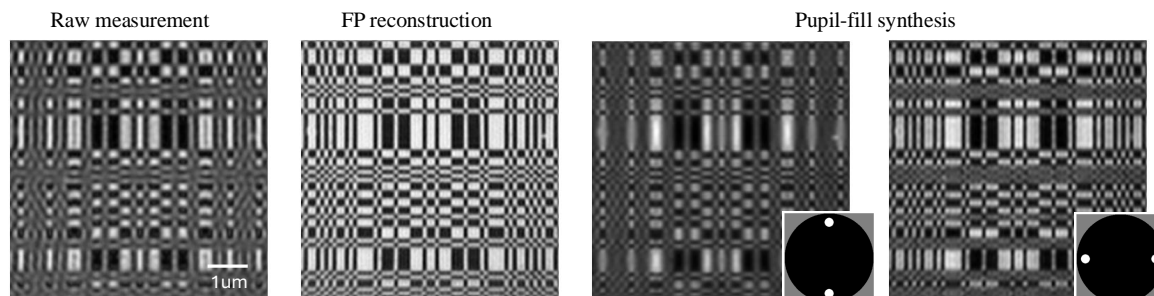


Figure 6. Pupil-fill synthesis using FP reconstruction. Left to right: (1) Raw measurement, (2) FP reconstruction, (3)-(4): Vertical dipole pupil-fill and horizontal dipole pupil-fill. The bottom-right insets show the corresponding illumination patterns.

4.3 Pupil-fill synthesis

Figure 6 demonstrates the ability to synthesize arbitrary illumination patterns using the complex-field FP reconstruction. To illustrate this capability, we synthesize two different pupil-fills in orthogonal directions: vertical dipole illumination and horizontal dipole illumination.

The data shows the anisotropic resolution enhancement associated with each illumination pattern. Vertical dipole illumination increases modulation for horizontal features. Conversely, horizontal dipole illumination increases modulation for vertical features. These results highlight the effectiveness of pupil-fill synthesis in selectively optimizing resolution for different feature orientations.

5. CONCLUSION

In this work, we demonstrate the application of Fourier Ptychography to EUV photomask imaging, with the capability to reconstruct in the presence of field-dependent aberrations for 1D and 2D patterns. By leveraging FP, we achieved a $1.8\times$ resolution enhancement (from 82 nm to 46 nm) across a $30\ \mu\text{m} \times 30\ \mu\text{m}$ field-of-view.

We evaluate various reconstruction algorithms, including Gerchberg Saxton, Embedded Pupil Function Recovery, Gauss-Newton, and Angular ptychographic imaging with closed-form method, and demonstrated that Gauss-Newton-based FP reconstructions provide superior robustness against systematic errors while enabling aberration correction. To optimize the reconstruction, we employ automatic differentiation and pupil function regularization, increasing contrast and extending the usable FOV into formerly aberrated regions. To address systematic errors, we modeled and corrected field-dependent illumination wave-vector shifts in the SHARP system, applying a first-order approximation and automatic differentiation-based optimization.

We also demonstrate that the complex-field FP reconstruction enables the emulation of arbitrary illumination patterns from a single FPM dataset. These results highlight FP as a powerful computational imaging technique for EUV mask imaging, capable of overcoming optical system limitations through computational aperture synthesis and phase retrieval. Future work may focus on extension to higher NA EUV systems, and integrating machine-learning-based aberration correction.

6. ACKNOWLEDGMENTS

Lawrence Berkeley National Lab and the Advanced Light Source are supported by the Office of Science, Office of Basic Energy Sciences, of the U.S. Department of Energy under Contract No. DE-AC02-05CH11231. Antoine Islegen-Wojdyla is supported by an Early Career Award in the X-Ray Instrumentation Program in the Science User Facility Division of the Office of Basic Energy Sciences of the U.S. Department of Energy. Laura Waller and Chaoying Gu are partially supported by STROBE: A National Science Foundation Science & Technology Center under Grant No. DMR 1548924, the ARPA-H DARTS program.

REFERENCES

- [1] Zheng, G., Horstmeyer, R., and Yang, C., “Wide-field, high-resolution Fourier ptychographic microscopy,” *Nature photonics* **7**(9), 739–745 (2013).
- [2] Ou, X., Horstmeyer, R., Yang, C., and Zheng, G., “Quantitative phase imaging via Fourier ptychographic microscopy,” *Optics letters* **38**(22), 4845–4848 (2013).
- [3] Horstmeyer, R., Chung, J., Ou, X., Zheng, G., and Yang, C., “Diffraction tomography with Fourier ptychography,” *Optica* **3**(8), 827–835 (2016).
- [4] Wakonig, K., Diaz, A., Bonnin, A., Stambanoni, M., Bergamaschi, A., Ihli, J., Guizar-Sicairos, M., and Menzel, A., “X-ray Fourier ptychography,” *Science advances* **5**(2), eaav0282 (2019).
- [5] Benk, M. P., Miyakawa, R. H., Chao, W., Wang, Y.-G., Wojdyla, A., Johnson, D. G., Donoghue, A. P., and Goldberg, K. A., “A broader view on EUV-masks: adding complementary imaging modes to the SHARP microscope,” *Proc. SPIE* **9235**, 92350K (2014).
- [6] Naulleau, P. P., Goldberg, K. A., Batson, P., Bokor, J., Denham, P., and Rekawa, S., “Fourier-synthesis custom-coherence illuminator for extreme ultraviolet microfield lithography,” *Appl. Opt.* **42**, 820–826 (Feb 2003).
- [7] Goldberg, K. A., Benk, M. P., Wojdyla, A., Mochi, I., Rekawa, S. B., Allezy, A. P., Dickinson, M. R., Cork, C. W., Chao, W., Zehm, D. J., Macdougall, J. B., Naulleau, P. P., and Rudack, A., “Actinic mask imaging: recent results and future directions from the SHARP EUV microscope,” *Proc. SPIE* **9048**, 90480Y (2014).
- [8] Goldberg, K. A., Mochi, I., Benk, M. P., Lin, C., Allezy, A. P., Dickinson, M., Cork, C. W., Macdougall, J. B., Anderson, E. H., Chao, W., et al., “The SEMATECH high-NA actinic reticle review project (SHARP) EUV mask-imaging microscope,” in [*Photomask Technology 2013*], **8880**, 95–103, SPIE (2013).
- [9] Wojdyla, A., Benk, M. P., Naulleau, P. P., and Goldberg, K. A., “EUV photolithography mask inspection using Fourier ptychography,” *Proceedings of SPIE* **10656**, 106560W (2018).
- [10] Ou, X., Zheng, G., and Yang, C., “Embedded pupil function recovery for Fourier ptychographic microscopy,” *Optics express* **22**(5), 4960–4972 (2014).
- [11] Tian, L., Li, X., Ramchandran, K., and Waller, L., “Multiplexed coded illumination for Fourier Ptychography with an LED array microscope,” *Biomedical optics express* **5**(7), 2376–2389 (2014).
- [12] Cao, R., Shen, C., and Yang, C., “High-resolution, large field-of-view label-free imaging via aberration-corrected, closed-form complex field reconstruction,” *arXiv preprint arXiv:2309.00755* (2023).
- [13] Yeh, L.-H., Dong, J., Zhong, J., Tian, L., Chen, M., Tang, G., Soltanolkotabi, M., and Waller, L., “Experimental robustness of Fourier ptychography phase retrieval algorithms,” *Optics Express* **23**(26), 33214–33240 (2015).
- [14] Kandel, S., Maddali, S., Allain, M., Hruszkewycz, S. O., Jacobsen, C., and Nashed, Y. S., “Using automatic differentiation as a general framework for ptychographic reconstruction,” *Optics Express* **27**(13), 18653–18672 (2019).
- [15] You, R. and Liang, R., “Self-calibrating Fourier ptychographic microscopy using automatic differentiation,” *Optics Letters* **50**(2), 415–418 (2025).
- [16] Zhao, Q., Wang, R., Zhang, S., Wang, T., Song, P., and Zheng, G., “Deep-ultraviolet Fourier ptychography (DUV-FP) for label-free biochemical imaging via feature-domain optimization,” *APL Photonics* **9**(9) (2024).
- [17] Lee, K. C., Chae, H., Xu, S., Lee, K., Horstmeyer, R., Lee, S. A., and Hong, B.-W., “Anisotropic regularization for sparsely sampled and noise-robust Fourier ptychography,” *Optics Express* **32**(14), 25343–25361 (2024).
- [18] Banterle, N., Bui, K. H., Lemke, E. A., and Beck, M., “Fourier ring correlation as a resolution criterion for super-resolution microscopy,” *Journal of Structural Biology* **183**(3), 363–367 (2013).
- [19] Goldberg, K. A., Mochi, I., Naulleau, P. P., Han, H., and Huh, S., “Benchmarking EUV mask inspection beyond 0.25 NA,” in [*Photomask Technology 2008*], **7122**, 774–781, SPIE (2008).
- [20] Yamazoe, K., Mochi, I., and Goldberg, K. A., “Gradient descent algorithm applied to wavefront retrieval from through-focus images by an extreme ultraviolet microscope with partially coherent source,” *J. Opt. Soc. Am. A* **31**, B34–B43 (Dec 2014).
- [21] Gunjala, G., Wojdyla, A., Sherwin, S., Shanker, A., Benk, M. P., Goldberg, K. A., Naulleau, P. P., and Waller, L., “Extreme ultraviolet microscope characterization using photomask surface roughness,” *Scientific reports* **10**(1), 11673 (2020).